Why the first magic-angle is different from others in twisted graphene bilayers: Interlayer currents, kinetic and confinement energy, and wave-function localization

Leonardo A. Navarro-Labastida ⓘ, Abdiel Espinosa-Champo ⓘ, Enrique Aguilar-Mendez ⓘ, and Gerardo G. Naumis ⓘ[*]
Departamento de Sistemas Complejos, Instituto de Física, Universidad Nacional Autónoma de México (UNAM),
Apartado Postal 20-364, 01000 CDMX, México

The chiral Hamiltonian for twisted graphene bilayers is analyzed in terms of its squared Hamiltonian which removes the particle-hole symmetry and thus one bipartite lattice, allowing us to write the Hamiltonian in terms of a 2×2 matrix. This brings to the front the three main physical actors of twisted systems: kinetic energy, confinement potential, and an interlayer interaction operator which is divided in two parts: a non-Abelian interlayer operator and an operator which contains an interaction energy between layers. Here, each of these components is analyzed as a function of the angle of rotation as well as in terms of the wave-function localization properties. It is proved that the non-Abelian operator represents interlayer currents between each layer of triangular sublattices, i.e., a second-neighbor interlayer current between bipartite sublattices. A crossover is seen between such contributions, and thus, the first magic-angle is different from other higher-order magic-angles. Such angles are determined by a balance between the negative energy contribution from interlayer currents and the positive contributions from the kinetic and confinement energies. A perturbative analysis performed around the first magic-angle allows us to explore analytically the details of such an energy balance.

I. INTRODUCTION

Twisted bilayer graphene (TBG) exhibits unconventional superconducting phases and Mott insulating states [1]. This discovery was made by working upon previous theoretical efforts which suggested a path to increase many-body interactions [2–4]. Bistritzer and MacDonald [2] found that, at certain twisting angles, TBG presents flat bands where the Fermi velocity goes to zero. Several works confirmed the existence of such flat bands at certain magic-angles where the electron-electron interactions are maximized [1,5].

However, there are still many open questions concerning this problem [6–11], even in the one-particle operator limit. For example, the wave function of TBG has been found to be reminiscent of a quantum Hall wave function in a torus, and this opens analogies to the physics of Landau levels [12–15], the Hofstadter butterfly [16–19], or the fractional quantum Hall effect [20]. There is also an interesting connection to topological phases, Moiré edge states, and Weyl semimetals [21–26].

Also, as the Moiré pattern generates a high electron density localization, interest in making quantum dots with TBG has been steadily increasing [27,28]. Other interesting applications have been found [13,29–37] as well as optical/electrical signatures [38,39]. The mobility/stability of electrons is influenced by the triangular geometry of the TBG [40–43]. Previous papers have studied nematicity [44–46], phonons/plasmons [6,47], disorder effects [48–50], and other important related properties [4,51–57]. However, a direct analytic connection with the presence of superconducting phases at magic-angles has not yet been achieved completely. As

expected, the interacting behavior of electrons in the Hubbard model is important to characterize the electronic correlations and their fermionic behavior [40,58–61].

An important mechanism in the properties of Moiré systems is the superlattice relaxation [62–64]. This is especially important near *AA* stacking points, where interlayer hopping tends to be reduced. Theoretically, when the hopping that couples layers in *AA* regions is tuned off, the system becomes exactly chiral symmetric [65]. This model shows a recurrence at magic-angles and reduces the problem to a more analytically manipulable Hamiltonian operator. For this reason, among others, the chiral Hamiltonian reduces the complexity of the continuum model and captures all the important symmetries and physics of TBG [65]. The mathematical properties and structure of the wave function have been rigorously studied in several works [14,66–69]. As one can imagine, the graphene layer has two triangular sublattices, each one with an equal magnetic flux but with opposite sign; therefore, TBG consists of coupled magnetic fluxes with opposite signs between layers [11,70,71]. This produces a strong skyrmion behavior in which electrons form vortices, reflected in the presence of strong electron-electron correlation on specific locations across the Moiré superlattice [72].

To further understand the physics behind the problem, in a previous work, we considered the squared Hamiltonian (SH) of the chiral model [73]. There are several interesting works in the literature on the SH in tight-binding models where important physical relationships have been found [74–80]. This procedure can be interpreted as transforming the Dirac equation into the Klein-Gordon equation. Relations with topological invariants in many-body systems [76] and higher-order topological phases [74,75] have also been studied, and more recently, the square-root topological phases related to SH have

────────
*naumis@fisica.unam.mx

been experimentally measured [81–83]. In the TBG model, the SH represents a renormalization that removes one of the bipartite triangular sublattices for each graphene layer [73,84–86]. In general, the physics of the SH is the same as that of the original Hamiltonian, but the renormalized operator allows us to see properties that in the original model were hidden or difficult to identify. For example, it reveals three physical driving mechanisms: kinetic energy, an effective confinement potential, and a non-Abelian gauge field leading to magnetic fields. It also allows us to write the Hamiltonian as a simple 2×2 operator and then use Pauli matrices in which topological properties are more evident. More importantly, it gives a direct physical interpretation of magic-angles in terms of the wave function geometrical frustration, i.e., we showed that such renormalization folds the spectrum around zero energy, and thus, zero-mode states correspond to antibonding ground states in a triangular lattice [73]. As is well known, antibonding states in triangular lattices are frustrated, as the wave function cannot achieve a phase difference of π between sites. This costs energy and usually pushes states into highly degenerate spectral regions and thus to a nearby depletion of states seen as gaps or pseudogaps [85–88]. In Ref. [73], we showed that magic-angles occur whenever the interlayer frustration is exactly zero. Then at magic-angles, a highly degenerated state is formed and separated by a gap from the rest of the spectrum. This effect is achieved by a very precise fine tuning of the wave function Fourier coefficients akin to the Hall effect. Notice that, although previous works showed some peculiarities about frustration properties [9,89,90], it was not clear why such states were at the middle of the band. The same happens with the analytical form of zero modes, which were identified as reminiscent of a Hall effect ground state without a clear explanation of why the lowest Landau level was found at the middle of the spectrum and not at its bottom end [11,65].

However, several spectral analyses hinted that the first magic-angle is different from the others [11,65,91]. For example, numerically, it was found that the spectrum of the TBG chiral model shows a remarkable $\frac{3}{2}$ recurrence rule for the magic-angles [65]; however, the first angle does not follow it, and the reason is not known. As we will see here, their wave function charge density and phases are remarkably different from others. Thus, it would be very useful to understand the reason why such behaviors differ from other magic-angles. For this reason, here, we present such an study. Also, this paper allows us to discern how the physical mechanisms scale between each other as the twist angle is changed.

The layout of this paper is the following. In Sec. II, we present the model to be studied and the identification of the main physical contributions to the problem. Then in Sec. III, we study the zero mode wave functions and their localization. In Sec. IV, we study the expectation values of each energy contribution and discuss the interlayer current contribution. In Sec. V, we show why the first magic-angle is different from the others. Finally, conclusions are given in the last section.

II. SQUARED TBG CHIRAL HAMILTONIAN

The chiral Hamiltonian of TBG is a variant of the original Bistritzer-MacDonald Hamiltonian in which the *AA* tunneling
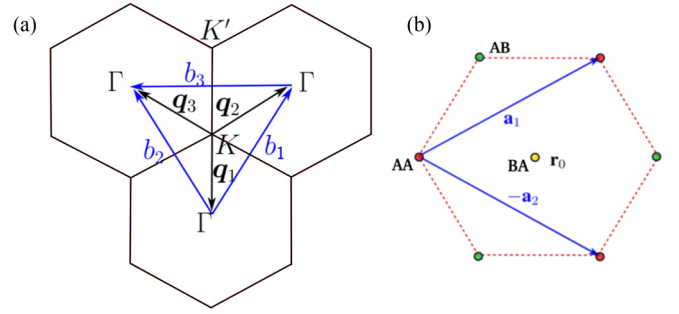

FIG. 1. (a) Moiré Brillouin zones (mBZs) in reciprocal space, $b_{1,2}$ are the base vectors. (b) Real-space Moiré unit cell, $\mathbf{a}_{1,2}$ are two Moiré lattice vectors. Point $\mathbf{r}_0 = (\mathbf{a}_1 - \mathbf{a}_2)/3$ is the *BA* stacking point where all components of the wave function vanish at magic α.

is set to zero [11]. We use as a basis the wave vectors $\Phi(r) = [\psi_1(r), \psi_2(r), \chi_1(r), \chi_2(r)]^T$, where the index 1, 2 represents each graphene layer, and $\psi_j(r)$ and $\chi_j(r)$ are the Wannier orbitals on each inequivalent site of the unit cell of graphene. The chiral Hamiltonian is given [65,92,93]:

$$\mathcal{H} = \begin{bmatrix} 0 & D^*(-r) \\ D(r) & 0 \end{bmatrix}, \tag{1}$$

where the zero-mode operator is defined as

$$D(r) = \begin{bmatrix} -i\bar{\partial} & \alpha U(r) \\ \alpha U(-r) & -i\bar{\partial} \end{bmatrix}, \tag{2}$$

and

$$D^*(-r) = \begin{bmatrix} -i\partial & \alpha U^*(-r) \\ \alpha U^*(r) & -i\partial \end{bmatrix}, \tag{3}$$

with $\bar{\partial} = \partial_x + i\partial_y$, and $\partial = \partial_x - i\partial_y$. The potential is

$$U(\mathbf{r}) = \exp(-i\mathbf{q}_1 \cdot \mathbf{r}) + \exp(i\phi)\exp(-i\mathbf{q}_2 \cdot \mathbf{r}) + \exp(-i\phi)\exp(-i\mathbf{q}_3 \cdot \mathbf{r}), \tag{4}$$

where the phase factor $\phi = 2\pi/3$, the Moiré lattice vectors are given by $\mathbf{q}_1 = k_\theta(0, -1)$, $\mathbf{q}_2 = k_\theta(\frac{\sqrt{3}}{2}, \frac{1}{2})$, and $\mathbf{q}_3 = k_\theta(-\frac{\sqrt{3}}{2}, \frac{1}{2})$, the Moiré modulation vector is $k_\theta = 2k_D \sin\frac{\theta}{2}$, $k_D = \frac{4\pi}{3a_0}$ is the magnitude of the Dirac wave vector, and a_0 is the lattice constant of monolayer graphene, see Fig. 1. The physics of this model is captured by the parameter α, defined as $\alpha = \frac{w_1}{v_0 k_\theta}$, where w_1 is the interlayer coupling of stacking *AB/BA* with value $w_1 = 110$ meV, and v_0 is the Fermi velocity with value $v_0 = \frac{19.81 eV}{2k_D}$. Notice that the Hamiltonian in Eq. (1) was originally written in Ref. [65] using units where $v_0 = 1$, and $k_\theta = 1$; thus, the operators ∂ and $\bar{\partial}$ are dimensionless. This allows us to treat the system with a fixed geometry for any twist angle as in these units $\mathbf{q}_1 = (0, -1)$, $\mathbf{q}_2 = (\frac{\sqrt{3}}{2}, \frac{1}{2})$, and $\mathbf{q}_3 = (-\frac{\sqrt{3}}{2}, \frac{1}{2})$. The twist angle thus only enters in the dimensionless parameter α.

By a renormalization procedure which consists of taking the square of H, we found that [73]

$$H^2 = \begin{bmatrix} -\nabla^2 + \alpha^2|U(-\mathbf{r})|^2 & \alpha A^\dagger(\mathbf{r}) \\ \alpha A(\mathbf{r}) & -\nabla^2 + \alpha^2|U(\mathbf{r})|^2 \end{bmatrix}. \tag{5}$$
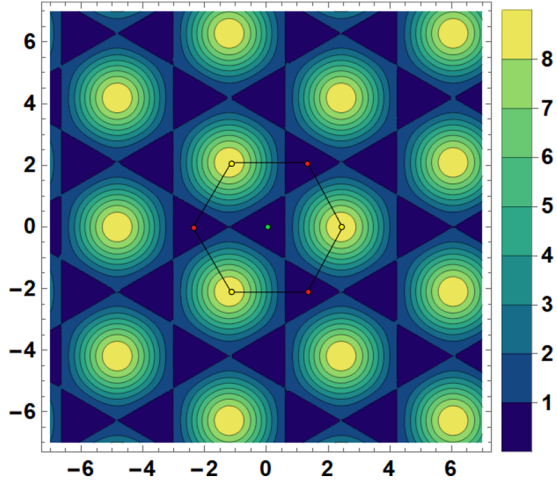
FIG. 2. Contour plot of the confinement potential $|U(\mathbf{r})|^2$ showing minima at *AA* (green) and *AB* (red) stacking points and maxima at *BA* stacking points (yellow). As a reference, the Wigner-Seitz cell of the Moiré lattice is indicated. For the first magic-angle, the **K** wave function tracks this potential.

The squared norm of the potential is an effective confinement potential:

$$|U(\mathbf{r})|^2 = 3 + 2\cos(\mathbf{b}_1 \cdot \mathbf{r} - \phi) + 2\cos(\mathbf{b}_2 \cdot \mathbf{r} + \phi)$$
$$+ 2\cos(\mathbf{b}_3 \cdot \mathbf{r} + 2\phi), \tag{6}$$

where $\mathbf{b}_{1,2} = \mathbf{q}_{2,3} - \mathbf{q}_1$ are the Moiré Brillouin zone (mBZ) vectors, and $\mathbf{b}_3 = \mathbf{q}_3 - \mathbf{q}_2$. In Fig. 2, we plot $|U(\mathbf{r})|^2$ in real space, with the Wigner-Seitz indicated. This effective potential has a hexagonal structure where the r_0 point in the *BA* stacking lays in the maximum point of this potential and the minimums lay in the *AA* and *AB* stacking points. The off-diagonal terms in H^2 are

$$A(\mathbf{r}) = -i \sum_{\mu=1}^{3} \exp(i\mathbf{q}_\mu \cdot \mathbf{r})(2\hat{\mathbf{q}}_\mu^\perp \cdot \nabla - 1), \tag{7}$$

and

$$A^\dagger(\mathbf{r}) = -i \sum_{\mu=1}^{3} \exp(-i\mathbf{q}_\mu \cdot \mathbf{r})(2\hat{\mathbf{q}}_\mu^\perp \cdot \nabla + 1), \tag{8}$$

where $\nabla^\dagger = -\nabla$ with $\nabla = (\partial_x, \partial_y)$ and $\mu = 1, 2, 3$. This is an essential point, as eigenvalues must be real [notice that $-A^\dagger(-\mathbf{r}) = A(\mathbf{r})$].

We also define the following operator which contains all the nondiagonal contributions:

$$\hat{A}(\mathbf{r}) = \begin{bmatrix} 0 & \alpha A^\dagger(\mathbf{r}) \\ \alpha A(\mathbf{r}) & 0 \end{bmatrix}. \tag{9}$$

Also, $\hat{\mathbf{q}}_\mu^\perp$ is a set of unitary vectors perpendicular to the set $\mathbf{q}_\mu$:

$$\hat{\mathbf{q}}_1^\perp = (1, 0), \qquad \hat{\mathbf{q}}_2^\perp = \left(-\frac{1}{2}, \frac{\sqrt{3}}{2}\right),$$
$$\hat{\mathbf{q}}_3^\perp = \left(-\frac{1}{2}, -\frac{\sqrt{3}}{2}\right). \tag{10}$$

The importance of this renormalization is that now we can see the three main ingredients of the problem: (i) the kinetic contribution via the ∇^2 term (which leads to frustration), (ii) a confinement potential $|U(\mathbf{r})|^2$ and, (iii) the interlayer interaction $A(\mathbf{r})$.

An important feature that we will further analyze is that $A(\mathbf{r})$ is made from two terms, and therefore, it is convenient to define separately the quantities:

$$A_g(\mathbf{r}) = -2i \sum_{\mu=1}^{3} \exp(i\mathbf{q}_\mu \cdot \mathbf{r})\hat{\mathbf{q}}_\mu^\perp \cdot \nabla$$
$$= 2 \sum_{\mu=1}^{3} \exp(i\mathbf{q}_\mu \cdot \mathbf{r})\hat{p}_\mu, \tag{11}$$

and

$$A_f(\mathbf{r}) = i \sum_{\mu=1}^{3} \exp(i\mathbf{q}_\mu \cdot \mathbf{r}), \tag{12}$$

where the dimensionless projected momentum operators are $\hat{p}_\mu = (\hat{\mathbf{q}}_\mu^\perp \cdot \hat{\boldsymbol{p}})$, as the dimensionless momentum operator is $\hat{\boldsymbol{p}} = -i\nabla$. See how Eq. (11) is akin to a Lorentz force term.

Let us also comment on some useful symmetries of $\mathcal{H}$, as they play important roles in the presence of flat bands [66,94]. For our purposes, the most important symmetry is the exact intravalley inversion symmetry [91] that produces flat bands and the chirality. The exact intravalley inversion symmetry operator is [91]

$$\mathcal{I} = \sigma_z \tau_y, \tag{13}$$

where the σ and τ operators are acting on the sublattice and layer degrees of freedom, respectively, and given by two different sets of Pauli matrices [91]. Using this definition, we have

$$\mathcal{I}\mathcal{H}(\mathbf{r})\mathcal{I}^\dagger = \mathcal{H}(-\mathbf{r}). \tag{14}$$

Our renormalized Hamiltonian also preserves this symmetry as

$$\mathcal{I}\mathcal{H}^2(\mathbf{r})\mathcal{I}^\dagger = \mathcal{H}^2(-\mathbf{r}). \tag{15}$$

For the chiral TBG, intravalley inversion follows from the $\mathcal{C}_2\mathcal{T}$ group symmetry, where $\mathcal{T}$ represents time reversal, and $\mathcal{C}_2$ is the cyclic group of order 2. The action of $\mathcal{C}_2\mathcal{T}$ is that of complex conjugates and exchanges the two sublattices. In the following section, we will further analyze the interplay between the different terms in H^2 and the role played by the symmetries.

III. WAVE FUNCTIONS: LOCALIZATION PROPERTIES

In this section, we discuss the localization properties of the zero-mode wave functions for different angles to see if there are differences between the first and higher-order magic-angles. We start with the Schrödinger equation $\mathcal{H}\Phi(r) = E\Phi(r)$. Considering only the first spinor component of $\Phi(r)$,

the explicit form of the zero-mode wave function is [65]

$$\begin{bmatrix} \psi_{\mathbf{k},1}(\mathbf{r}) \\ \psi_{\mathbf{k},2}(\mathbf{r}) \end{bmatrix} = \sum_{m,n} \begin{bmatrix} a_{mn} \\ b_{mn} \exp(i\mathbf{q}_1 \cdot \mathbf{r}) \end{bmatrix}$$

$$\times \exp[i(\mathbf{K}_{mn} + \mathbf{k}) \cdot \mathbf{r}], \qquad (16)$$

where a_{mn} and b_{mn} represents the Fourier coefficients of each spinor component representing layers 1 and 2, respectively, and $\mathbf{K}_{mn} = m\mathbf{b}_1 + n\mathbf{b}_2$, where $\mathbf{b}_{1,2} = \mathbf{q}_{2,3} - \mathbf{q}_1$ are the Moiré Brillouin zone vectors, and $\mathbf{b}_3 = \mathbf{q}_3 - \mathbf{q}_2$.

For the flat bands, it has been proved that [65]

$$\begin{bmatrix} \psi_{\mathbf{k},1}(\mathbf{r}) \\ \psi_{\mathbf{k},2}(\mathbf{r}) \end{bmatrix} = f_{\mathbf{k}}(z) \begin{pmatrix} \psi_{\mathbf{K},1} \\ \psi_{\mathbf{K},2} \end{pmatrix}, \qquad (17)$$

where $z = x + iy$. Here, $f_{\mathbf{k}}(z)$ is given in terms of Jacobi ϑ functions [65] or alternatively as a Weierstrass σ function [91]. Therefore, the electronic density for layer $j = 1, 2$ is $\rho_{\mathbf{k},j}(\mathbf{r}) = |f_{\mathbf{k}}(z)|^2 \rho_{\mathbf{K},j}(\mathbf{r})$ with $\rho_{\mathbf{K},j}(\mathbf{r}) = \psi_{\mathbf{K},j}^\dagger(\mathbf{r})\psi_{\mathbf{K},j}(\mathbf{r})$.

As the analytic form of $f_{\mathbf{k}}(z)$ is known, our interest here is focused on the study of $\Psi_K(\mathbf{r})$ which corresponds to the ground state of H^2 at *all angles*.

In Fig. 3, we present the resulting $\rho_{\mathbf{K}}(\mathbf{r})$ plots in real space at the first magic-angles and for each layer component, obtained by plugging Eq. (16) into $\mathcal{H}$ to obtain recurrence relations for a_{mn} and b_{mn}. As expected, $\rho_{\mathbf{K}}(\mathbf{r})$ present the rotational C_3 symmetry. Several features are worth noticing: (i) the first magic-angle is different from the others, as the amplitude is centered at the *AA* stacking points; (ii) it tracks the form of the $|U(\mathbf{r})|^2$ confining potential; and (iii) at other angles, the density is confined at somewhat similar locations but never at *AA* points as in the first one.

At the first magic-angle $\alpha_1 = 0.586$, one can use perturbation theory [65] to obtain the density (see the Appendix):

$$\rho_{\mathbf{K},1}(\mathbf{r})$$

$$= 1 + \frac{4\alpha^2}{\sqrt{3}} \sum_{\mu=1}^{3} \sin\left[\phi + (-1)^{\mu-1}\mathbf{b}_\mu \cdot \mathbf{r}\right]$$

$$+ \frac{2\alpha^4}{3} \left\{ 3 + 2C(\mathbf{r}) - \sum_{\mu=1}^{3} \cos\left[2\phi + 2(-1)^{\mu-1}\mathbf{b}_\mu \cdot \mathbf{r}\right] \right.$$

$$\left. + 2\cos\left[2\phi + (-1)^\mu \mathbf{b}_\mu \cdot \mathbf{r}\right] \right\}, \qquad (18)$$

where $C(\mathbf{r}) = \cos\left[(\mathbf{b}_1 + \mathbf{b}_2) \cdot \mathbf{r}\right] + \cos\left[(\mathbf{b}_1 - \mathbf{b}_3) \cdot \mathbf{r}\right] + \cos\left[(\mathbf{b}_2 + \mathbf{b}_3) \cdot \mathbf{r}\right]$, and the other component

$$\rho_{\mathbf{K},2}(\mathbf{r}) = \alpha^2 \left[3 + 2\sum_{\mu=1}^{3} \cos(\mathbf{b}_\mu \cdot \mathbf{r}) \right], \qquad (19)$$

This solution allows us to understand the coincidence between Fig. 2 and the first angle in Fig. 3, as basically the $\rho_{\mathbf{K},2}(\mathbf{r})$ is proportional to the confinement potential.

In Fig. 4, the real and imaginary parts of the wave function for each layer are shown, and the Wigner-Seitz cell is indicated as well. The wave functions present vortices, but the most important feature to be seen in Fig. 4 is the lack of vortices for the component 1 at the first magic-angle as well as for the component 2 in the *AA* stacking point. Such features are in agreement with the perturbative solution for such an angle.
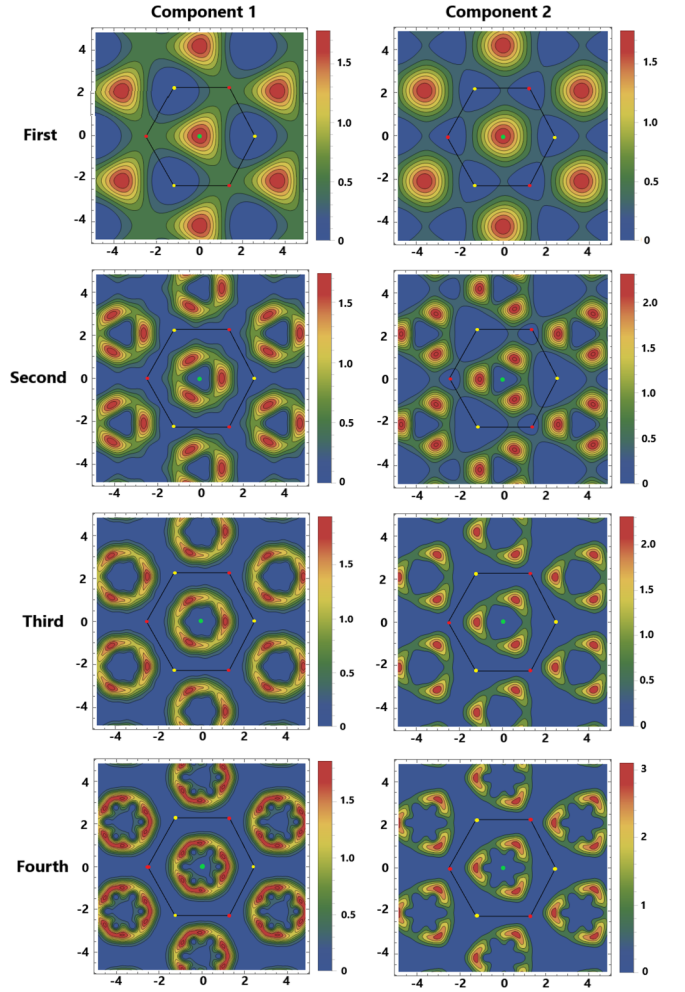

FIG. 3. Density in real space for the Dirac point K wave function on each layer for the first four magic-angles $\alpha = 0.586, 2.221, 3.751,$ and 5.276 in the unit cell of the real space representation. The *AA* (green), *AB* (red), and *BA* (yellow) points are indicated. As a reference, the Wigner-Seitz cell of the Moiré lattice is indicated. Notice how the first angle is different from the others, as the *AA* stacking points concentrate the density.

Although at this moment there are not published figures of the phases to compare with, intralayer currents present vortices [91]. However, the vortices of such currents do not coincide with the wave function vortices, a feature to be expected since they are made from a sum of different $\mathbf{k}$ points wave functions. Theoretically, it has been suggested that the pairing of the wave function vortices is a special signature of the TBG from which superconductivity arises [70]. Here, what is most important for us is the very different behavior of the phases and density associated with the first magic-angle when compared with others.

To further highlight such differences, in Fig. 5, we plot the amplitude of the Fourier coefficients a_{mn} and b_{mn} for each layer. Again, we see that the first magic-angle is remarkably different from the others, as its main Fourier component contributions are around the origin. However, for the second, third, and fourth magic-angles, there is a hole at $\mathbf{k} \approx 0$. This hole appears at $\alpha \approx 1$. Also, when $\alpha \to \infty$, both layers have nearly the same spectral behavior of the Fourier components.
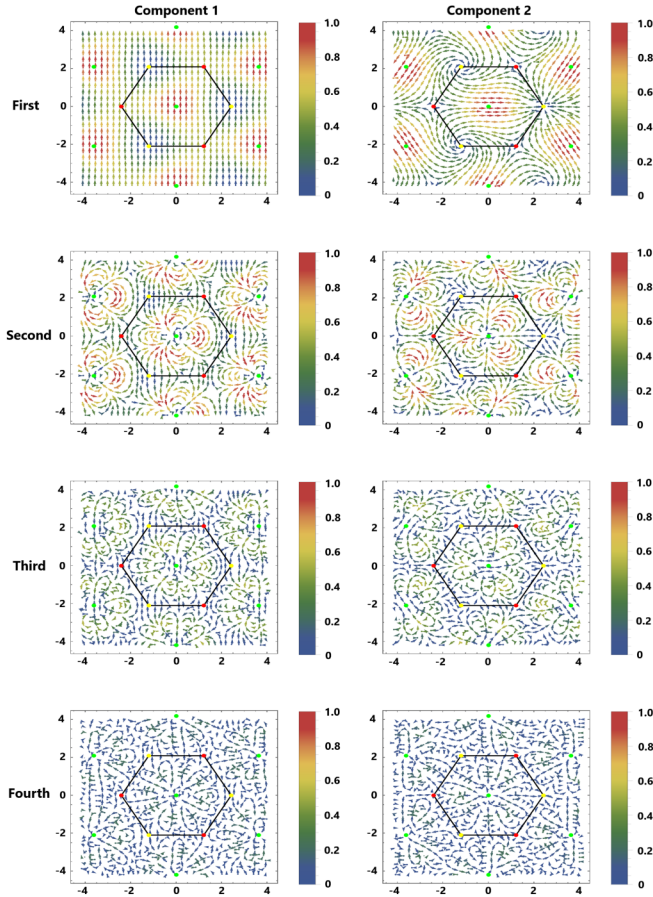
FIG. 4. Phases in real space where the vertical component of the vectors corresponds to $\mathrm{Im}(\psi_{1,2})$ and the horizontal component to $\mathrm{Re}(\psi_{1,2})$, in the Dirac point K wave function on each layer, for the first four magic-angles $\alpha = 0.586,\ 2.221,\ 3.751,$ and 5.276 in the unit cell of the real space representation. The color code is the corresponding wave function amplitude. The AA (green), AB (red), and BA (yellow) points are indicated. As a reference, the Wigner-Seitz cell of the Moiré lattice is indicated. Notice how the first angle is different from the others, as the localization occurs at the AA stacking points.

The Fourier components of $\Psi(\mathbf{r})$ in general form complex patterns. However, as seen in Fig. 5, at the K, K' points most of the coefficients a_{mn} and b_{mn} are negligible, and the Fourier spectrum consists of six localized peaks forming hexagonal patterns for high values of α. Moreover, we find that, at the lth magic-angle α_l, the main contributions of the coefficients a_{mn} are given by $(m, n) = (\pm l, 0)$, $(0, \pm l)$, and $(\pm l, \mp l)$. Notably, l has been associated with a Landau-level index [91].

As the wave functions in reciprocal space change but keep a well-localized peak, this means that the localization behavior is far from trivial. To test numerically this observation, here, we measure the localization by using a inverse participation ratio (IPR) [95–97]:

$$\mathrm{IPR}_l(\alpha) = \int_m |\psi_l(\mathbf{r})|^4 d^2 r, \qquad (20)$$

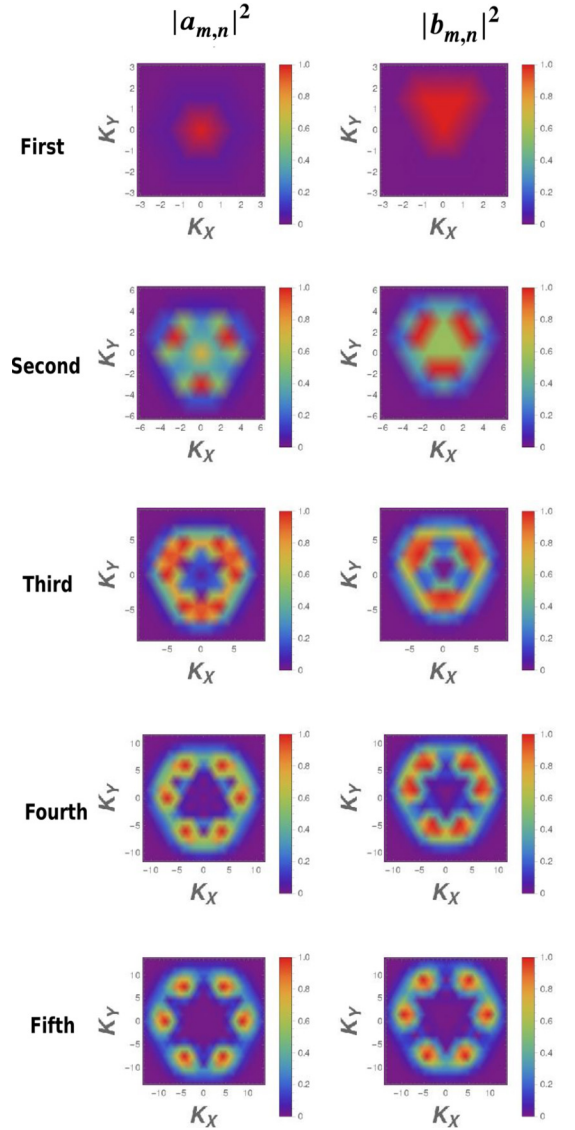where $l = 1, 2$ is the index of the top and bottom component of the spinor.

FIG. 5. Fourier coefficients of the two spinor components for the **K** valley wave function. Right and left columns correspond to the layer 1 (a_{mn}) and layer 2 (b_{mn}) coefficients, respectively. The color represents the amplitude of the coefficient $|a_{m,s}|^2$ or $|b_{m,s}|^2$ in the hexagonal reciprocal lattice centered at location (k_x, k_y). Here, we plot their spectral square magnitude for the first five magic-angles $\alpha_1 = 0.586$, $\alpha_2 = 2.221$, $\alpha_3 = 3.751$, $\alpha_4 = 5.276$, and $\alpha_5 = 6.795$.

In Fig. 6, we present the IPR for each layer, analyzing the behavior of the IPR for the top and bottom component. In the limit $\alpha \to 0$, the IPR reproduces the expected solution $(1, 0)$. In the interval $\alpha \in [0, \alpha_1]$, the wave function ψ_1 becomes less delocalized, while ψ_2 becomes more localized. When α increases, there is an oscillation in the IPR_1 and IPR_2. Magic-angles occur at inflexion points or at minima, and there is a tendency to increase the overall localization in both layers when $\alpha \to \infty$.

Surprisingly, the IPR for magic-angles is the same for all states in the flat band as, except at the poles,

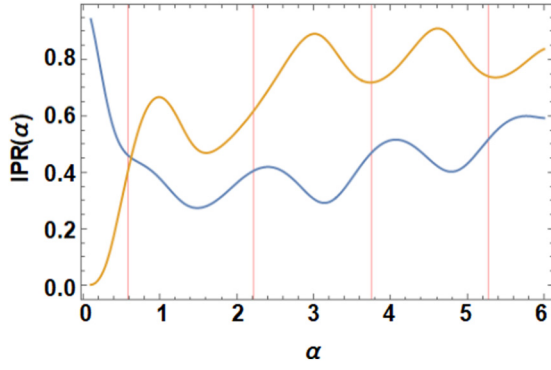$$|f_{\mathbf{k}}(z)|^2 = 1, \qquad (21)$$

FIG. 6. Inverse participation ratio (IPR) as a function of α for the top (blue) and bottom (brown) components of the twisted bilayer graphene (TBG) wave function at $\mathbf{k} = \mathbf{K}$. The red vertical lines indicate the first four magic-angles. Notice how the first magic-angle is different from the others, as in fact, the IPR of both layers is nearly the same.

even though $f_{\mathbf{k}}(z)$ is a complex meromorphic function. The reason for this relation comes from the normalization of any state corresponding to the flat band, as we must have

$$\int_m \rho_{\mathbf{k}}(\mathbf{r})d^2r = \int_m |f_{\mathbf{k}}(z)|^2 \rho_{\mathbf{K}}(\mathbf{r})d^2r = 1, \quad (22)$$

where m denotes integration over the mBZ. Then we observe that the wave function for $\mathbf{k} = \mathbf{K}$ is also normalized, from which it follows that, to be consistent, we must have $|f_{\mathbf{k}}(z)|^2 = 1$ [notice that the poles of $f_{\mathbf{k}}(z)$ are canceled out by the zeros of $\psi_{\mathbf{K}}(\mathbf{r})$]. We have verified numerically that this condition is true.

To summarize the results of this section, again, there are clear signatures in the wave functions that the first magic-angle is different from the others.

IV. EXPECTATION VALUES AND INTERLAYER CURRENTS

To understand the contribution of each physical driving term in the SH and why the first magic-angle is different, we next calculate the expected value of each corresponding operator in H^2. From the eigenvalue equation $H^2\Psi_{\mathbf{k}}(\mathbf{r}) = E(\mathbf{k})^2\Psi_{\mathbf{k}}(\mathbf{r})$, where $\Psi = [\psi_{\mathbf{k},1}(\mathbf{r}), \psi_{\mathbf{k},2}(\mathbf{r})]$, and using Eq. (5):

$$\sum_{j=1}^2 (\langle T_j \rangle + \langle V_j \rangle) + \langle \hat{A} \rangle = E^2(\mathbf{k}), \quad (23)$$

where the expected values for a given layer $j = 1, 2$ are

$$\langle T_j \rangle \equiv -\int_m \psi_{\mathbf{k},j}^\dagger(\mathbf{r})\nabla^2\psi_{\mathbf{k},j}(\mathbf{r})d^2\mathbf{r}, \quad (24)$$

$$\langle V_j \rangle \equiv \alpha^2 \int_m |U(\mp\mathbf{r})|^2 \rho_{\mathbf{k},j}(\mathbf{r})d^2\mathbf{r}, \quad (25)$$

and $\langle \hat{A} \rangle = \langle A^\dagger \rangle + \langle A \rangle$, with

$$\langle A^\dagger \rangle \equiv \alpha \int_m \psi_{\mathbf{k},1}^\dagger(\mathbf{r})A^\dagger(\mathbf{r})\psi_{\mathbf{k},2}(\mathbf{r})d^2\mathbf{r}, \quad (26)$$

and

$$\langle A \rangle \equiv \alpha \int_m \psi_{\mathbf{k},2}^\dagger(\mathbf{r})A(\mathbf{r})\psi_{\mathbf{k},1}(\mathbf{r})d^2\mathbf{r}. \quad (27)$$

Notice that $\langle A^\dagger \rangle$ and $\langle A \rangle$ are not exactly properly defined expected values, as they involve the bracket of two different wave function components, and thus, they can becomplex values or not. However, the total contribution expected value of the whole off-diagonal terms is real. The total kinetic energy is $\langle T \rangle = \langle T_1 \rangle + \langle T_2 \rangle$, while the total confinement energy is

$$\langle V \rangle = \langle V_1 \rangle + \langle V_2 \rangle \leqslant \frac{8\pi^2}{\sqrt{3}}\alpha^2, \quad (28)$$

where the last bound is obtained using the wave function normalization.

To understand how $\langle \hat{A} \rangle$ depends on the two contributions coming from the off-diagonal terms in H^2, we will define the space-dependent expected value of the gradient terms in Eq. (5) as

$$\mathcal{A}_g(\mathbf{r}) = (\psi_1^* \quad \psi_2^*)\begin{bmatrix} 0 & \alpha A_g^\dagger(\mathbf{r}) \\ \alpha A_g(\mathbf{r}) & 0 \end{bmatrix}\begin{pmatrix} \psi_1 \\ \psi_2 \end{pmatrix}, \quad (29)$$

which come from the nondiagonal, gradient part of H^2:

$$\hat{A}_g = \begin{bmatrix} 0 & \alpha A_g^\dagger(\mathbf{r}) \\ \alpha A_g(\mathbf{r}) & 0 \end{bmatrix}. \quad (30)$$

Therefore,

$$\mathcal{A}_g(\mathbf{r}) = -2i\alpha \sum_\mu \hat{\mathbf{q}}_\mu^\perp$$
$$\cdot [\exp(i\mathbf{q}_\mu \cdot \mathbf{r})\psi_1\nabla\psi_2^*$$
$$+ \exp(-i\mathbf{q}_\mu \cdot \mathbf{r})\psi_2^*\nabla\psi_1]. \quad (31)$$

By adding its complex conjugate, we obtain that

$$\mathcal{A}_g(\mathbf{r}) + \mathcal{A}_g^*(\mathbf{r}) = 2\alpha\frac{m}{e\hbar}\sum_\mu \hat{\mathbf{q}}_\mu^\perp$$
$$\cdot [\exp(-i\mathbf{q}_\mu \cdot \mathbf{r})\mathbf{j}_{12}$$
$$+ \exp(i\mathbf{q}_\mu \cdot \mathbf{r})\mathbf{j}_{21}], \quad (32)$$

where we defined the interlayer currents as

$$\mathbf{j}_{12} = \frac{ie\hbar}{2m}(\psi_1\nabla\psi_2^* - \psi_2^*\nabla\psi_1), \quad (33)$$

and

$$\mathbf{j}_{21} = \frac{ie\hbar}{2m}(\psi_2\nabla\psi_1^* - \psi_1^*\nabla\psi_2). \quad (34)$$

Such definitions are unusual, as they involve two different wave functions from each layer and only one sublattice. Thus, this requires some comments and thoughts. In recent papers, Wang *et al.* [91,98] and Wang and Liu [99] proposed a somewhat analogous definition for a second-neighbor intralayer current, i.e., these authors defined

$$\mathbf{j}_{ss} = \frac{ie\hbar}{2m}(\psi_s\nabla\psi_s^* - \psi_s^*\nabla\psi_s), \quad (35)$$

where $s = 1, 2$. This definition is required, as the usual current is obtained from $\partial_x H$, which turns out to be zero in the ground state. Therefore, they defined a current in one of the bipartite
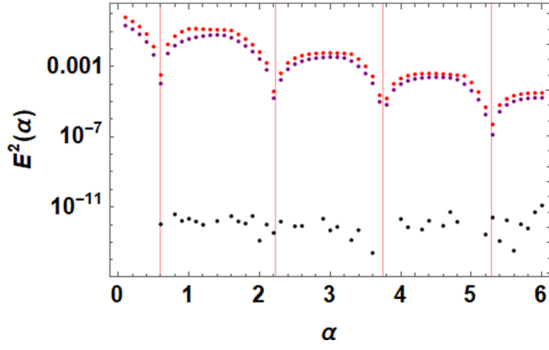
FIG. 7. $E^2(\mathbf{k})$ obtained from the squared Hamiltonian in Eq. (5) at the Dirac K (black), Γ (red), and a generic ζ (purple) point where the red vertical lines indicate the first four magic-angles.

lattices, as can be seen by performing a tight-binding calculation of the intralayer orbital current. Here, we do not need to appeal to such a recourse, as the square Hamiltonian initially renormalized the hexagonal lattice in a triangular lattice, and therefore, the second neighborhood interaction is implicit in the renormalization procedure. In Ref. [91], it was argued that, if j_{ss} is discretized in a tight-binding Hamiltonian, we have that $j_{ss} = i(a_{s,i}^{\dagger} a_{s,j} - a_{s,j}^{\dagger} a_{s,i})$, where $a_j^{\dagger}$ and a_j create and annihilate, respectively, electrons in site j. In a similar way, if in Eq. (31) we discretize the spinor component gradient, we have that $i(\psi_1 \nabla \psi_2^* - \psi_2^* \nabla \psi_1) \rightarrow i(a_{2,j}^{\dagger} a_{1,i} - a_{2,i}^{\dagger} a_{1,j})$ and the other current component as $i(\psi_2 \nabla \psi_1^* - \psi_1^* \nabla \psi_2) \rightarrow i(a_{1,j}^{\dagger} a_{2,i} - a_{1,i}^{\dagger} a_{2,j})$. Therefore, this leads to the interpretation of an interlayer current.

Let us now integrate over the primitive cell to get the expected value of the current. By noting that $\langle \hat{A}_g \rangle = \langle \hat{A}_g \rangle^*$, it follows that

$$\langle \hat{A}_g \rangle = 2\alpha \sum_{\mu} \hat{\mathbf{q}}_{\mu}^{\perp} \cdot \langle \tilde{\mathbf{j}}_{12}(\mathbf{q}_{\mu}) + \tilde{\mathbf{j}}_{21}(-\mathbf{q}_{\mu}) \rangle, \qquad (36)$$

where $\tilde{\mathbf{j}}_{12}(\mathbf{q}_{\mu}) = \int e^{-i\mathbf{q}_{\mu} \cdot \mathbf{r}} \mathbf{j}_{12}(\mathbf{r}) d^2\mathbf{r}$, and $\tilde{\mathbf{j}}_{21}(-\mathbf{q}_{\mu}) = \int e^{i\mathbf{q}_{\mu} \cdot \mathbf{r}} \mathbf{j}_{21}(\mathbf{r}) d^2\mathbf{r}$. Therefore, $\langle \hat{A}_g \rangle$ is just the sum of the Fourier components of the current at the points $\mathbf{q}_1$, $\mathbf{q}_2$, and $\mathbf{q}_3$. In a similar way, the space-dependent expected value of the second ingredient of $\langle A(\mathbf{r}) \rangle$ is

$$\mathcal{A}_f(\mathbf{r}) = i\alpha \sum_{\mu} [\psi_2^* \psi_1 \exp(i\mathbf{q}_{\mu} \cdot \mathbf{r}) - \psi_1^* \psi_2 \exp(-i\mathbf{q}_{\mu} \cdot \mathbf{r})], \qquad (37)$$

where $\mathcal{A}_f(\mathbf{r}) = \mathcal{A}_f^*(\mathbf{r})$, and we define the operator:

$$\hat{A}_f = \begin{bmatrix} 0 & \alpha A_f^{\dagger}(\mathbf{r}) \\ \alpha A_f(\mathbf{r}) & 0 \end{bmatrix}. \qquad (38)$$

V. EXPECTATION VALUES AND CURRENTS AT DIFFERENT k POINTS

In this section, we study all contributions defined in the previous section as a function of the twist at representative points in $\mathbf{k}$ space. One is the Γ point, which reveals how magic-angles arise, and the other is the K point, which is the ground state for all α. Figure 7 shows such behavior as obtained from the numerical simulation, i.e., the top of the
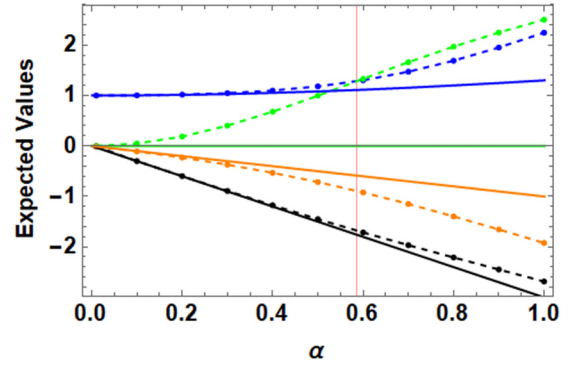

FIG. 8. Expected values in the Γ point vs α. The numerical results are indicated with dashed lines and points. The kinetic energy $\langle T \rangle$ is in blue, confinement energy $\langle V \rangle$ green, $\langle \hat{A}_g^{\dagger} \rangle$ black, and $\langle \hat{A}_f^{\dagger} \rangle$ orange. The solid lines are the perturbative solutions (see Appendix).

band $E^2(\Gamma)$ goes to zero at the magic-angles, while $E^2(\mathbf{K})$ is the ground state. The $\mathbf{k} = \zeta$ point, chosen at random in the mBZ, lies inside this interval.

A. Revealing the magic-angles: Γ point expected values

From Fig. 7, we see that $E^2(\Gamma)$ can be used to reveal the magic-angles, as it always gives the highest energy of the first H^2 band. For a flat band to exist, the energy $E^2(\Gamma)$ must be zero.

For the Γ point, it is very illustrative to use perturbation theory in the limit $\alpha \rightarrow 0$. As shown in the Appendix, up to linear order in α, we have that

$$\langle T \rangle = 1, \qquad \langle V \rangle = 0, \qquad (39)$$

$$\langle \hat{A}_g \rangle = -3\alpha, \qquad \langle \hat{A}_f \rangle = -\alpha. \qquad (40)$$

It follows that

$$\langle T + V \rangle + \langle \hat{A}_f \rangle + \langle \hat{A}_g \rangle = 1 - 4\alpha \approx E^2(\Gamma). \qquad (41)$$

In Fig. 8, we present a comparison between these expected values and the numerical results, showing a good agreement for $\langle T \rangle$, $\langle \hat{A}_f \rangle$, and $\langle \hat{A}_g \rangle$, as $\alpha \rightarrow 0$. For $\langle V \rangle$, the agreement is not so good, as this requires higher-order perturbation terms. The previous approximation allows us to make a crude estimate of the first magic-angle as

$$E(\Gamma) \approx \pm\sqrt{|1 - 4\alpha|}. \qquad (42)$$

Therefore, $\alpha_1 \approx \frac{1}{4}$, a value below $\alpha_1 = 0.586$. Higher-order terms in the expansion are needed to increase the accuracy, but the main principle behind a magic-angle is already present in this simple approach. Further confirmation is provided in Fig. 9, where we show numerically how magic angles arise whenever the curve $\langle T + V \rangle$ intersects $|\langle \hat{A} \rangle|$.

Then we conclude that, in going from $\alpha = 0$ to α_1, the confinement potential starts to contribute and reaches the kinetic energy at the magic-angle. The off-diagonal operators always diminish the energy. As expected, the first magic-angle is thus produced when the sum of the kinetic plus confinement energies are equal in magnitude to the expected values of the off-diagonal operators. The particularity here is that, for α_1, we have $\langle A_g \rangle / \langle A_f \rangle \approx 3$.
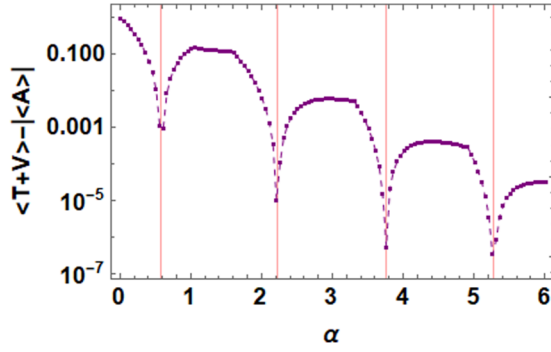
FIG. 9. Numerical calculation of $\langle T + V \rangle - |\langle \hat{A} \rangle|$ vs α at the **Γ** point for the first four magic-angles. For all magic-angles, $|\langle \hat{A} \rangle| = \langle T + V \rangle$.

The numerical results in Fig. 9 show how the same principle applies for other magic-angles, as $\langle T + V \rangle - |\langle \hat{A} \rangle|$ goes to zero. However, as seen in Fig. 10, for $\alpha \gg \alpha_1$, the current term $\langle \hat{A}_g \rangle$ dominates over $\langle \hat{A}_f \rangle$, and in fact, $\langle \hat{A}_f \rangle$ can be neglected, as we will discuss in the following subsection. Notice also the jumps associated to each α_n, possibly related with Landau levels. The other particularity is that $\langle T \rangle \approx \langle V \rangle$, as $\alpha \to \infty$; thus, in Fig. 9, one cannot distinguish one from the other in this scale.

B. Ground state: *K* point

The point $\mathbf{k} = \mathbf{K}$ is a ground state for any α. Let us have some general considerations about it. As $\langle T_j \rangle \geqslant 0$ and $\langle V_j \rangle > 0$, it follows that, for $E^2 = 0$, we have that $\langle A^\dagger \rangle \leqslant 0$ and $\langle A \rangle \leqslant 0$. Figure 11 numerically confirms these results. Other interesting features are seen. The first is already clear from Eq. (23): for the ground state $E^2 = 0$ and due to symmetry, we obtain

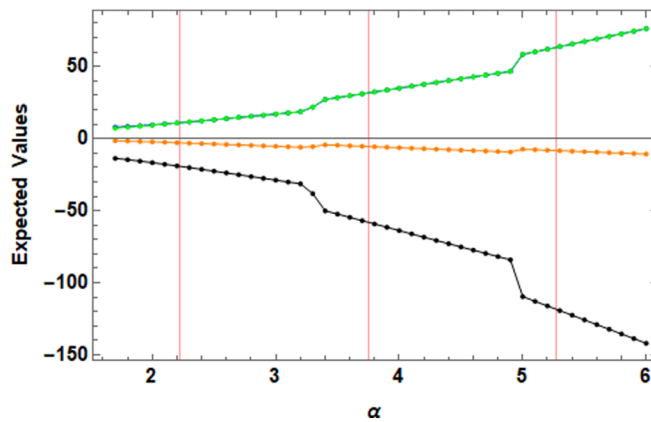$$\langle T_1 \rangle + \langle V_1 \rangle = -\langle A^\dagger \rangle, \tag{43}$$

FIG. 10. Expected values in the **Γ** point vs α. Kinetic energy $\langle T \rangle$ (blue), confinement energy $\langle V \rangle$ (green), $\langle \hat{A}_g^\dagger \rangle$ (black), and $\langle \hat{A}_f^\dagger \rangle$ (orange). Notice that the kinetic and confinement energies are of the same order; thus, it is not possible to distinguish the blue curve in this scale. The vertical red lines are the second, third, and fourth magic-angles.
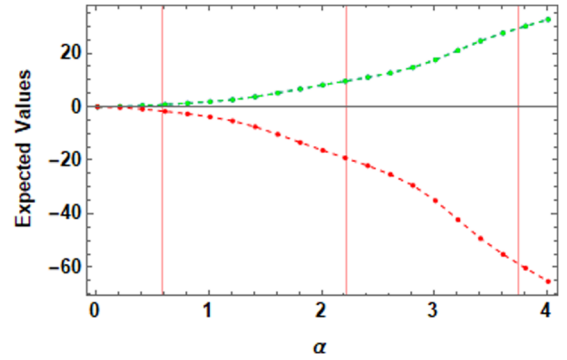

FIG. 11. Expected value contributions of the energy as a function of α at the Dirac point $\mathbf{k} = \mathbf{K}$, $\langle T \rangle$ (blue), $\langle V \rangle$ (green), and $\langle \hat{A} \rangle$ (red). As for any angle $\langle T \rangle = \langle V \rangle$, the blue symbols are hidden by the green ones. The conservation of energy implied by Eq. (47) is satisfied as the kinetic, confinement, and interlayer contributions always sum zero.

and

$$\langle T_2 \rangle + \langle V_2 \rangle = -\langle A \rangle. \tag{44}$$

The derivation that follows is made by considering a symmetrized basis [73]. In this case, there is no way to distinguish the upper and lower layers except for a relative phase; it follows that we must have $\langle T_1 \rangle = \langle T_2 \rangle$ and $\langle V_1 \rangle = \langle V_2 \rangle$. As the general flat-band solutions are given by [91]

$$\Psi(\mathbf{r}) = \begin{bmatrix} \psi_1(\mathbf{r}) \\ \psi_2(\mathbf{r}) \end{bmatrix} = \begin{bmatrix} g(\mathbf{r}) \\ ig(-\mathbf{r}) \end{bmatrix} \times \Phi_k(\mathbf{r}), \tag{45}$$

where $g(\mathbf{r})$ is a Bloch wave function, and $\Phi_k(\mathbf{r})$ is the quantum Hall wave function of the lowest Landau level, we replace this wave function into the expressions for $\langle A \rangle$ and $\langle A^\dagger \rangle$ to show that

$$\langle A^\dagger \rangle = \langle A \rangle. \tag{46}$$

This is a reminiscent condition of the intravalley symmetry of Eq. (1). Therefore, for the total kinetic energy and total confinement energy, we have that

$$\langle \hat{A} \rangle = 2\langle A^\dagger \rangle = 2\langle A \rangle = -\langle T \rangle - \langle V \rangle. \tag{47}$$

Using the bound for the confinement energy, we find that $\langle \hat{A} \rangle$ is bounded by

$$|\langle \hat{A} \rangle| \leqslant \langle T \rangle + \frac{8\pi^2}{\sqrt{3}} \alpha^2. \tag{48}$$

Figure 11 further confirms Eqs. (47) and (48). Also, in Fig. 12, we compare the numerical results with the perturbative approach up to second order in α, as detailed in the Appendix. The agreement is excellent and allows us to (i) further confirm analytically Eq. (47) in the limit $\alpha \to 0$ and (ii) test the validity of the numerical approach.

From the previous results, it is clear that $\langle A \rangle$ will always diminish with α to compensate the increased value of the confinement and kinetic terms. However, this interlayer interaction depends on two terms, as in the Γ point. This requires further analysis.

In Fig. 13, we present the interlayer current for $\mathbf{k} = \mathbf{K}$ in real space. The vector directions represent the polar angle
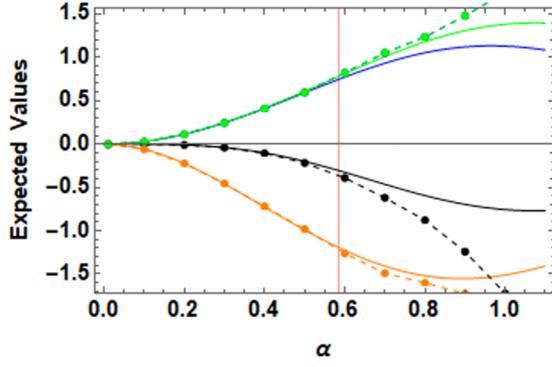
FIG. 12. Zoom of the operator expected values vs α for the region $\alpha << 1$. The filled circles were obtained from the numerical simulation at the Dirac point $\mathbf{K} = 0$, corresponding to kinetic energy $\langle T \rangle$ (blue), confinement $\langle V \rangle$ (green), interlayer current $\langle \hat{A}_g \rangle$ (black), and averaged interlayer interaction $\langle \hat{A}_f \rangle$ (orange). Notice that the numerical data for $\langle T \rangle$ are the same as $\langle V \rangle$, and thus, blue circles are not seen. The solid curves were obtained from the analytic perturbative expressions for the operator expected values up to second order in α (see Appendix). The same color code as in the numerical data was used for the curves. The red vertical line indicates the first magic-angle $\alpha_1 = 0.586$.

defined by the real and imaginary parts of $\mathcal{A}_f(\mathbf{r})$ or $\mathcal{A}_g(\mathbf{r})$. For the first magic-angle $\alpha = 0.586$, $\mathcal{A}_f(\mathbf{r})$ has more density in the AA stacking point, while $\mathcal{A}_g(\mathbf{r})$ has more current around the BA/AB stacking points. On the other hand, for the second magic-angle $\alpha = 2.221$, $\mathcal{A}_f(\mathbf{r})$ and $\mathcal{A}_g(\mathbf{r})$ have three points of high intensity inside the Wigner-Seitz cell. Also, it is interesting to note that, in the AA/AB stacking points, there is a vortex behavior, as those seen in Fig. 4.
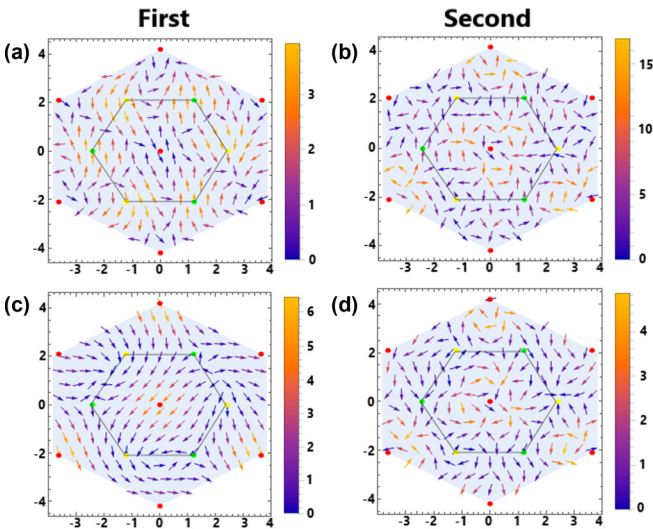

FIG. 13. Interlayer contributions in the real space at the Dirac point $\mathbf{k} = \mathbf{K}$ corresponding to (a) and (b) $\mathcal{A}_g(\mathbf{r})$ and (c) and (d) $\mathcal{A}_f(\mathbf{r})$ for the two first magic-angles $\alpha = 0.586$ and 2.221. The arrows indicate the direction of the field and the color code the intensity. The stacking points AA (red), AB (green), and BA (yellow) are indicated in the Moiré Wigner-Seitz unit cell.
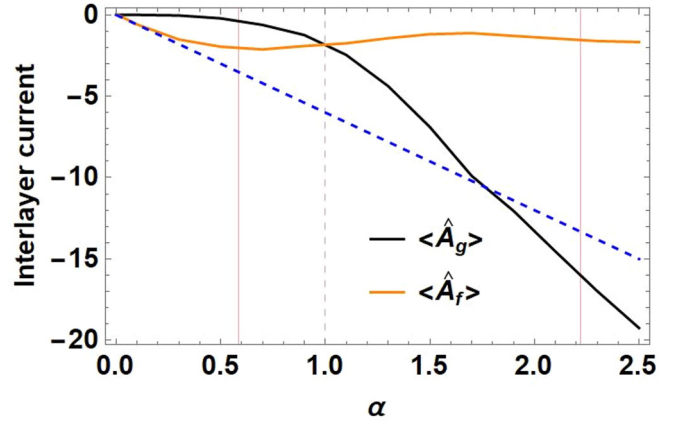

FIG. 14. Components of the interlayer operator $\langle \hat{A}(\alpha) \rangle$ as a function of α at the $\mathbf{K}$ point. The two first magic-angles $\alpha = 0.586$ and 2.221 are indicated with the red vertical lines. At $\alpha \approx 1$ $\langle \hat{A}_g \rangle = \langle \hat{A}_f \rangle$, while the blue dashed line indicates the theoretical lower bound for $\langle \hat{A}_f \rangle \geqslant -6\alpha$.

Using the spinor symmetry in Eq. (45) and integrating over the primitive cell, it follows that

$$\langle \hat{A}_f \rangle = -2\alpha \Im \sum_\mu \int \psi_2^* \psi_1 \exp(i\mathbf{q}_\mu \cdot \mathbf{r}) d^2\mathbf{r}$$

$$= -\alpha \sum_\mu \mathrm{Im}\big[\tilde{\psi}_2^*(q_\mu) \circledast \tilde{\psi}_1(q_\mu) \big], \qquad (49)$$

where $\circledast$ means a convolution, and $\tilde{\psi}_s$ is the Fourier transform of ψ_s.

In Fig. 14, we show the evolution of Eqs. (36) and (49). Clearly, for the first magic-angle, $\langle \hat{A}_g \rangle$ and $\langle \hat{A}_f \rangle$ have similar magnitudes but become radically separated after the first magic-angle, i.e., $\langle \hat{A}_g \rangle \gg \langle \hat{A}_f \rangle$. Therefore, the term $\langle \hat{A}_f \rangle$ is only relevant for $\alpha < 1$, making the first magic-angle different from others, as in the Γ point. The reason for this change is easy to see, as $\langle \hat{A}_f \rangle$ is bounded by the norm of the wave functions, and thus,

$$|\langle \hat{A}_f \rangle| \leqslant 6\alpha, \qquad (50)$$

a fact further corroborated by using Eq. (45) to find its explicit form:

$$\langle \hat{A}_f \rangle = -\alpha \sum_\mu \int g^*(\mathbf{r}) g(-\mathbf{r}) |\Phi_k(\mathbf{r})|^2 \cos(\mathbf{q}_\mu \cdot \mathbf{r}) d^2\mathbf{r}. \quad (51)$$

Meanwhile, $\langle \hat{A}_g \rangle$ is proportional to the gradient $\nabla \psi_j$ which is not bounded by $\rho(\mathbf{r})$.

Further confirmation is obtained by looking at the perturbative solution (see Appendix). Here, $\langle T \rangle = \langle V \rangle \approx 3\alpha^2(1 - \alpha^2)$, while $\langle \hat{A}_g \rangle = -6\alpha^4(1 + 2\alpha^2)$, and $\langle \hat{A}_f \rangle = -6\alpha^2(1 + 2\alpha^2)$. Then $\langle \hat{A}_g \rangle / \langle \hat{A}_f \rangle \approx \alpha^2$. This ratio goes from zero at $\alpha = 0$ to 1 at $\alpha = 1$.

C. Comparison between different k points

The previous analysis was made for $\mathbf{k} = \mathbf{K}$. In Figs. 15 and 16, we extend the analysis for other flat-band states at magic-angles. Figure 15 presents $\langle \hat{A}_g \rangle$ and $\langle \hat{A}_f \rangle$ in reciprocal space.
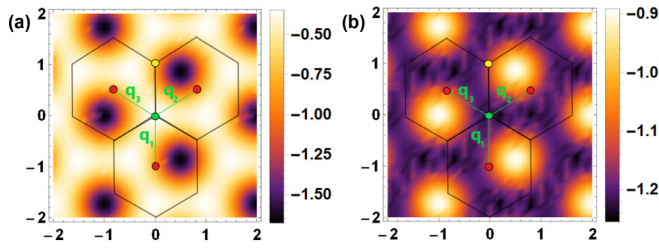
FIG. 15. Components of the interlayer current mean values as a function of momentum. (a) corresponds to $\langle \hat{A}_g \rangle$, and (b) corresponds to $\langle \hat{A}_f \rangle$ at the first magic-angle $\alpha = 0.586$. The Moiré Brillouin zone (mBZ) is indicated where $\mathbf{q}_1$, $\mathbf{q}_2$, and $\mathbf{q}_3$ are the Moiré lattice vectors, and the high symmetry points $\mathbf{\Gamma}$ (red), $\mathbf{K}'$ (yellow), and $\mathbf{K}$ (green) also are indicated.

For the first magic-angle $\alpha = 0.586$, the term $\langle \hat{A}_g \rangle$ is maximal where $\langle \hat{A}_f \rangle$ is minimal; both have similar magnitude range. On the other hand, for higher magic-angles, the reciprocal space structure of $\langle \hat{A}_g \rangle$ and $\langle \hat{A}_f \rangle$ preserve the same behavior; however, $\langle \hat{A}_g \rangle$ has a substantially increased magnitude compared with $\langle \hat{A}_f \rangle$. If $\alpha \to \infty$, $\langle \hat{A}_g \rangle \gg \langle \hat{A}_f \rangle$. As a consequence, the analysis made for $\mathbf{k} = \mathbf{K}$ can be safely extended for all flat-band states.

Therefore, $\langle \hat{A}_f \rangle$ is only relevant for $\alpha < 1$ making the first magic-angle different from the others. As said before, $\langle \hat{A}_f \rangle$ is limited by $\rho(\mathbf{r})$, while $\langle \hat{A}_g \rangle$ is proportional to the wave function gradient. Moreover, as the IPR baseline increases, as seen in Fig. 6, gradients grow. However, in principle, the overlap between the gradient in one layer and the other layer wave function can diminish. As $\langle \hat{A}_g \rangle$ is proportional to α, to test the gradient effects, in Fig. 16, we plot $\langle \hat{A}_g \rangle / \alpha$. This indicates that currents $\mathbf{j}_{ss}$ due to gradients are the responsible for the effect. This behavior is also reflected in Fig. 5, as in the crossover $\alpha \approx 1$, the Fourier coefficients develop a hole around $\mathbf{k} = 0$. Notice in Fig. 16 that the magic-angles fall inside basins. This effect is especially prominent for non-high-symmetry points, as the ζ point, a fact that will be discussed in a forthcoming publication.
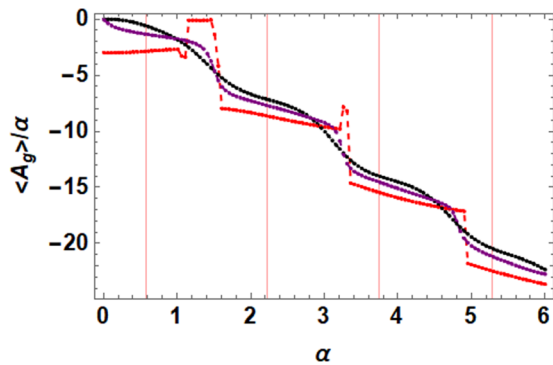

FIG. 16. Scaled interlayer current mean values $\langle \hat{A}_g \rangle / \alpha$ vs α for different representative points in $\mathbf{k}$ space: Γ (red curve), K (black curve), and ζ (magenta curve). This last point is chosen at the rim of the black spots of Fig. 15. Notice that $\langle \hat{A}_g \rangle$ is made from two elements: an overall decreasing behavior and, at the same time, basins separated by local maxima. Each magic-angle is associated with a basin.

Summarizing, the term $\langle \hat{A}_g \rangle$ is an energy associated with interlayer current leakage between bipartite sublattices, i.e., at second neighbors. Meanwhile, $\langle \hat{A}_f \rangle$ is a weighted average energy associated with overlaps between layers. The interlayer current magnitude grows as the rotation angle goes to zero, a fact due to the ever-increasing spatial gradients of the electron wave function.

VI. CONCLUSIONS

In this paper, we presented a theoretical and numerical analysis of the chiral TBG Hamiltonian using a renormalized Hamiltonian that removes the particle-hole symmetry, allowing us to identify the main physical elements of the problem and leading to a simple 2×2 matrix operator. Then we studied the electron localization in the TBG. We found numerically that the first magic-angle is different from the others, as the ground state wave function basically tracks the shape of the confinement potential. We calculated the localization using the IPR where magic-angles are revealed. Interestingly, we proved that all states in the flat band for magic-angles have the same participation ratio. We also evaluated the contributions from the kinetic energy, confinement energy, and interlayer interaction for the Γ and K points. These contributions were found using perturbation theory and numerically. A good agreement between both was found. Our analysis shows that the Γ point reveals how a magic-angle arises.

We found that the first magic-angle in the Γ point occurs when (1) the confinement and kinetic energies are the same, (2) the off-diagonal operator is the sum of kinetic and confinement energy, and (3) the intralayer current is bigger that the off-diagonal interaction energy term although not negligible. At other magic-angles, the balance is dictated only by the kinetic, confinement, and interlayer current. Therefore, interlayer currents are mainly responsible for bands to shrink.

In other works, the magic-angle effects have been associated with the effects of a space-dependent magnetic field [91,93,100,101]. Our results are in agreement with this idea, as the interlayer current can also be interpreted as a Lorentz force too. However, H^2 allowed us to identify the source of this field: the current between the underlying triangular sublattices of graphene.

It is tempting to try to identify our results with some geometrical feature of the twist angle. However, α contains both the geometry and the scale of the energy interaction. Here, we found that both are needed to make the confinement reach the kinetic energy and produce a strong interlayer current. For very big angles, confinement is just too weak. This is confirmed by the IPR which, at the first magic-angle, has the same value on each layer. We can also argue that the remarkable $\frac{3}{2}$ rule in the recurrence of α happens in the limit when $\langle \hat{A}_g \rangle \gg \langle \hat{A}_f \rangle$, as for higher magic-angles the nodal structure of the lowest Landau level does not depend significantly on the Moiré unit cell flux.

APPENDIX A: PERTURBATIVE ANALYSIS OF EXPECTED VALUES

1. H^2 at the Γ point

Consider the limit $\alpha \to 0$ for the Γ point. The corresponding wave function was found in Ref. [65]:

$$
\begin{aligned}
\psi_{\Gamma,1}(\mathbf{r}) = &\, U(-\mathbf{r}) + \frac{\alpha}{3} U(2\mathbf{r}) \\
&+ \frac{\alpha^2}{18}\Big[(2 - e^{i\phi})U(-\sqrt{7}\mathbf{R}_\gamma \mathbf{r}) \\
&+ (2 - e^{-i\phi})U(-\sqrt{7}\mathbf{R}_{-\gamma} \mathbf{r}) - 4U(2\mathbf{r})\Big] \\
&+ \cdots
\end{aligned} \tag{A1}
$$

and $\psi_{\Gamma,2}(\mathbf{r}) = i\mu_\alpha \psi_{\Gamma,1}(-\mathbf{r})$, where $R_\gamma \mathbf{r}$ is a counterclockwise rotation on angle γ, with $\tan(\gamma) = \frac{\sqrt{3}}{5}$, and $\mu_\alpha = \pm 1$; the minus sign is used for odd magic-angles. The normalization factor is

$$
N = \sum_{j=1}^{2} \int_m \psi_{\Gamma,j}^*(\mathbf{r})\psi_{\Gamma,j}(\mathbf{r})d^2r. \tag{A2}
$$

In this case, it is instructive to analyze first how H^2 operates on the wave function. Consider, for example, one of the differential equations resulting from Eq. (5):

$$
\begin{aligned}
[-\nabla^2 + \alpha^2|U(-\mathbf{r})|^2]\psi_{\Gamma,1}(\mathbf{r}) \\
+ \alpha A^\dagger(\mathbf{r})\psi_{\Gamma,2}(\mathbf{r}) = E^2\psi_{\Gamma,1}(\mathbf{r}),
\end{aligned} \tag{A3}
$$

where the square of energy E^2 is also expanded in powers of α, i.e., $E^2 = E_0^2 + \alpha E_1^2 + \alpha^2 E_2^2 + \dots$. Next, we use the relationship between wave functions on different layers:

$$
\begin{aligned}
[-\nabla^2 + \alpha^2|U(-\mathbf{r})|^2]\psi_{\Gamma,1}(\mathbf{r}) \\
+ i\mu_\alpha \alpha A^\dagger(\mathbf{r})\psi_{\Gamma,1}(-\mathbf{r}) = E^2\psi_{\Gamma,1}(\mathbf{r}),
\end{aligned} \tag{A4}
$$

If we collect terms up to order α using Eq. (A1), two equations are obtained. The zero order equation is

$$
-\nabla^2 U(-\mathbf{r}) = E_0^2 U(-\mathbf{r}), \tag{A5}
$$

and at order α,

$$
\begin{aligned}
-\tfrac{1}{3}\nabla^2 U(2\mathbf{r}) + i\mu_\alpha A^\dagger(\mathbf{r})U(\mathbf{r}) \\
= E_0^2 \tfrac{1}{3} U(2\mathbf{r}) + E_1^2 U(-\mathbf{r}).
\end{aligned} \tag{A6}
$$

From Eq. (A5), we recover E_0 as

$$
-\nabla^2 U(-\mathbf{r}) = -\nabla^2 \sum_{l=1}^{3} \exp(i\mathbf{q}_l \mathbf{r}) \exp[i(l-1)\phi]
$$

$$
= \sum_{l=1}^{3} |\mathbf{q}_l|^2 \exp(i\mathbf{q}_l \mathbf{r}) \exp[i(l-1)\phi], \tag{A7}
$$

and using $|\mathbf{q}_l|^2 = 1$, we prove that Eq. (A5) is indeed true whenever $E_0 = 1$, in agreement with Ref. [65].

Now consider Eq. (A6). As we did for the order zero component, is easy to show that

$$
-\nabla^2 U(2\mathbf{r}) = 4U(2\mathbf{r}). \tag{A8}
$$

Next, we compute $A^\dagger(\mathbf{r})U(\mathbf{r})$ using the two operators $A_g^\dagger(\mathbf{r})$ and $A_f^\dagger(\mathbf{r})$. Using the definition for $A_f^\dagger(\mathbf{r})$ and $U(\mathbf{r})$, we have

$$
A_f^\dagger(\mathbf{r})U(\mathbf{r}) = -i\sum_{l,s} \exp[-i(\mathbf{q}_l + \mathbf{q}_s)\mathbf{r}] \exp[i(s-1)\phi], \tag{A9}
$$

and the sum term is then divided in terms with $l = s$ and $l \neq s$:

$$
\sum_{l,s \neq l} \exp[-i(\mathbf{q}_l + \mathbf{q}_s)\mathbf{r}] \exp[i(s-1)\phi]
$$

$$
+ \sum_l \exp(-i2\mathbf{q}_l \mathbf{r}) \exp[i(l-1)\phi]. \tag{A10}
$$

Using that $\mathbf{q}_1 + \mathbf{q}_2 + \mathbf{q}_3 = 0$ and defining a new index $n = 6 - (l + s)$:

$$
\sum_{l,s \neq l} \exp[-i(\mathbf{q}_l + \mathbf{q}_s)\mathbf{r}] \exp[i(s-1)\phi]
$$

$$
= -\sum_n \exp(i\mathbf{q}_n \mathbf{r}) \exp[i(n-1)\phi]. \tag{A11}
$$

From the definition of $U(\mathbf{r})$, we finally obtain

$$
A_f^\dagger(\mathbf{r})U(\mathbf{r}) = -i[U(2\mathbf{r}) - U(-\mathbf{r})]. \tag{A12}
$$

Let us now consider the operator $A_g^\dagger(\mathbf{r})$ action. We have

$$
\begin{aligned}
A_g^\dagger(\mathbf{r})U(\mathbf{r}) = -i\sum_l \exp(-i\mathbf{q}_l \mathbf{r})2\mathbf{q}_l^\perp \\
\times \nabla\left\{\sum_s \exp(-i\mathbf{q}_s \mathbf{r}) \exp[i(s-1)\phi]\right\},
\end{aligned} \tag{A13}
$$

from which

$$
\begin{aligned}
A_g^\dagger(\mathbf{r})U(\mathbf{r}) = -\sum_{l,s \neq l} \exp[-i(\mathbf{q}_l + \mathbf{q}_s)\mathbf{r}] \\
\times \exp[i(s-1)\phi](2\mathbf{q}_l^\perp \cdot \mathbf{q}_s).
\end{aligned} \tag{A14}
$$

Next, we use that $\mathbf{q}_l^\perp \cdot \mathbf{q}_s = (-1)^{\zeta_{P(l,s)}} \frac{\sqrt{3}}{2}$, where $\zeta_{P(l,s)}$ is the sign of the permutation of the indices l and s, $+1$ for even and -1 for odd. Each pair permutation is obtained from the usual cyclic order $\{1, 2, 3\}$, so for example, $\mathbf{q}_1^\perp \cdot \mathbf{q}_2 = \frac{\sqrt{3}}{2}$, while $\mathbf{q}_2^\perp \cdot \mathbf{q}_1 = -\frac{\sqrt{3}}{2}$. Again, we use $\mathbf{q}_1 + \mathbf{q}_2 + \mathbf{q}_3 = 0$:

$$
\begin{aligned}
A_g^\dagger(\mathbf{r})U(\mathbf{r}) = \sqrt{3}\sum_{l,s>l} (-1)^{\zeta_{P(l,s)}} \\
\times \exp(i\mathbf{q}_n \mathbf{r})\{\exp[i(s-1)\phi] \\
- \exp[i(l-1)\phi]\},
\end{aligned} \tag{A15}
$$

where $n = 6 - (l + s)$. Finally,

$$
A_g^\dagger(\mathbf{r})U(\mathbf{r}) = 3iU(-\mathbf{r}). \tag{A16}
$$

Then we collect all the previous results inside Eq. (A6) using $\mu_\alpha = -1$ to confirm that the wave vector is an eigenvector

of H^2:

$$\frac{4}{3}U(2\mathbf{r}) - [U(2\mathbf{r}) - U(-\mathbf{r}) - 3U(-\mathbf{r})]$$
$$= E_1^2 U(-\mathbf{r}) + \frac{1}{3}U(2\mathbf{r}), \tag{A17}$$

i.e., comparing terms, we get $E_1^2 = 4$.

The previous analysis confirms that the solutions of H are also eigenfunctions of H^2. Now we find the expected values of each operator and for the corresponding differential equation. We start with the kinetic energy in the first layer:

$$\langle T_1 \rangle = -\frac{1}{N} \int_m d^2\mathbf{r} \Big[U^*(-\mathbf{r}) + \frac{\alpha}{3} U^*(2\mathbf{r}) \Big]$$
$$\times \nabla^2 \Big[U(-\mathbf{r}) + \frac{\alpha}{3} U(2\mathbf{r}) \Big]. \tag{A18}$$

Using Eqs. (A5) and (A8) and that $U^*(2\mathbf{r})$ and $U(-\mathbf{r})$ are orthogonal due to symmetry, the contribution of order α is zero, from which $\langle T_1 \rangle = \frac{1}{2}$. Now considering the contribution from the equation that results from the second row of Eq. (5), we have $\langle T_1 \rangle = \langle T_2 \rangle$. Then up to order α:

$$\langle T \rangle = \langle T_1 \rangle + \langle T_2 \rangle = 1. \tag{A19}$$

In a similar way, as $U^*(2\mathbf{r})$ and $U(-\mathbf{r})$ are orthogonal:

$$\langle V \rangle = \langle V_1 \rangle + \langle V_2 \rangle = 0. \tag{A20}$$

Finally, the other operators are

$$\langle \hat{A}_f^\dagger \rangle = -\alpha, \tag{A21}$$

while

$$\langle \hat{A}_g^\dagger \rangle = -3\alpha. \tag{A22}$$

It follows that

$$\langle T \rangle + \langle V \rangle + \langle \hat{A}_f^\dagger \rangle + \langle \hat{A}_g^\dagger \rangle = 1 - 4\alpha \approx E^2. \tag{A23}$$

In Fig. 8, we compare the previous results with the numerical simulation, obtaining a good agreement, as $\alpha \to 0$.

2. H^2 at the K point

Here, we consider a perturbative solution of Eq. (A24) for $\alpha \to 0$ in the K point, as was found in Ref. [65]:

$$\Psi_{\mathbf{K}}(\mathbf{r}) = \begin{bmatrix} \psi_{\mathbf{K},1}(\mathbf{r}) \\ \psi_{\mathbf{K},2}(\mathbf{r}) \end{bmatrix}$$
$$= \begin{bmatrix} 1 + \alpha^2 u_2(\mathbf{r}) + \alpha^4 u_4(\mathbf{r}) \cdots \\ \alpha u_1(\mathbf{r}) + \alpha^3 u_3(\mathbf{r}) + \cdots \end{bmatrix}. \tag{A24}$$

Considering only terms up to order α^2, we get

$$u_1(\mathbf{r}) = -i[\exp(i\mathbf{q}_1 \cdot \mathbf{r}) + \exp(i\mathbf{q}_2 \cdot \mathbf{r})$$
$$+ \exp(i\mathbf{q}_3 \cdot \mathbf{r})], \tag{A25}$$

$$u_2(\mathbf{r}) = \frac{-i}{\sqrt{3}} \exp(-i\phi)$$
$$\times [\exp(-i\mathbf{b}_1 \cdot \mathbf{r}) + \exp(i\mathbf{b}_2 \cdot \mathbf{r})$$
$$+ \exp(-i\mathbf{b}_3 \cdot \mathbf{r})] + \text{c.c.} \tag{A26}$$

These functions must be normalized before calculating the expected values. The normalization factor is

$$N = \frac{8\pi^2}{3\sqrt{3}} \Big(1 + 3\alpha^2 + 2\alpha^4 + \frac{6}{7}\alpha^6 + \frac{107}{98}\alpha^8 + \cdots \Big). \tag{A27}$$

With these expressions for ψ_1 and ψ_2, we obtain

$$\int \psi_2^*(\mathbf{r}) \exp(i\mathbf{q}_u \cdot \mathbf{r}) \psi_1(\mathbf{r}) d^2\mathbf{r} = \frac{8i\pi^2(\alpha + \alpha^3)}{3\sqrt{3}N}, \tag{A28}$$

and

$$\int \psi_1^*(\mathbf{r}) \exp(-i\mathbf{q}_u \cdot \mathbf{r}) \psi_2(\mathbf{r}) d^2\mathbf{r} = -\frac{8i\pi^2(\alpha + \alpha^3)}{3\sqrt{3}N}, \tag{A29}$$

for $\mu = 1, 2, 3$. Therefore, considering an extra α and i factor from the operator definition, we have

$$\langle \hat{A}_f \rangle \approx \frac{-6(\alpha^2 + \alpha^4)}{1 + 3\alpha^2 + 2\alpha^4 + \frac{6}{7}\alpha^6 + \frac{107}{98}\alpha^8}. \tag{A30}$$

This result is in agreement with the predicted bound found in Eq. (50). Consider in the same limit the other operator. We have that

$$-2i \int \psi_2^*(\mathbf{r}) \exp(-i\mathbf{q}_u \cdot \mathbf{r}) \hat{\mathbf{q}}_\mu^\perp \cdot \nabla \psi_1(\mathbf{r}) d^2\mathbf{r} = -\frac{8\pi^2 \alpha^3}{3\sqrt{3}N}, \tag{A31}$$

and the terms containing $\exp(i\mathbf{q}_u \cdot \mathbf{r})\psi_1^*(\mathbf{r})\hat{\mathbf{q}}_\mu^\perp \cdot \nabla \psi_2(\mathbf{r})$ give the same result. This confirms Eq. (46), i.e., $\langle A \rangle = \langle A^\dagger \rangle$. By collecting terms, we finally obtain that

$$\langle \hat{A}_g \rangle \approx \frac{-6\alpha^4}{\left(1 + 3\alpha^2 + 2\alpha^4 + \frac{6}{7}\alpha^6 + \frac{107}{98}\alpha^8 \right)}. \tag{A32}$$

Next, we find the expected values of the kinetic and confining potential operators to confirm the theoretical and numerical analysis. Using that

$$\int \psi_1^*(\mathbf{r}) \nabla^2 \psi_1(\mathbf{r}) d^2\mathbf{r} = -\frac{16\pi^2 \alpha^4}{\sqrt{3}N}, \tag{A33}$$

$$\int \psi_2^*(\mathbf{r}) \nabla^2 \psi_2(\mathbf{r}) d^2\mathbf{r} = -\frac{8\pi^2 \alpha^2}{\sqrt{3}N}, \tag{A34}$$

and

$$\int \psi_1^*(\mathbf{r}) |U(-\mathbf{r})|^2 \psi_1(\mathbf{r}) d^2\mathbf{r} = \frac{8\pi^2(3 + 2\alpha^2)}{3\sqrt{3}N}, \tag{A35}$$

$$\int \psi_2^*(\mathbf{r}) |U(\mathbf{r})|^2 \psi_2(\mathbf{r}) d^2\mathbf{r} = \frac{16\pi^2 \alpha^2}{\sqrt{3}N}, \tag{A36}$$

it follows that

$$\langle V \rangle \approx \frac{3\alpha^2 + 6\alpha^4 + 2\alpha^6}{1 + 3\alpha^2 + 2\alpha^4 + \frac{6}{7}\alpha^6 + \frac{107}{98}\alpha^8}, \tag{A37}$$

and for the kinetic energy term,

$$\langle T \rangle \approx \frac{3(\alpha^2 + 2\alpha^4)}{1 + 3\alpha^2 + 2\alpha^4 + \frac{6}{7}\alpha^6 + \frac{107}{98}\alpha^8}. \tag{A38}$$

By expanding the denominators, we arrive to the final perturbative expectation values:

$$\langle T \rangle \approx 3\alpha^2 - 3\alpha^4, \tag{A39}$$

$$\langle V \rangle \approx 3\alpha^2 - 3\alpha^4, \tag{A40}$$

and

$$\langle \hat{A}_f \rangle \approx -6\alpha^2 + 12\alpha^4, \tag{A41}$$

$$\langle \hat{A}_g \rangle \approx -6\alpha^4 + 18\alpha^6, \tag{A42}$$

in agreement with $\langle V \rangle = \langle T \rangle > 0$. Also, $\langle V \rangle + \langle T \rangle + \langle A \rangle \approx 0$ up to order α^4. In Fig. 12, we plot Eqs. (A40)–(A42) and compare them with the numerical results obtained from finding numerically the eigenstates of the Hamiltonian.

[1] Y. Cao, V. Fatemi, S. Fang, K. Watanabe, T. Taniguchi, E. Kaxiras, and P. Jarillo-Herrero, Nature (London) **556**, 43 (2018).

[2] R. Bistritzer and A. H. MacDonald, Proc. Natl. Acad. Sci. USA **108**, 12233 (2011).

[3] J. M. B. Lopes dos Santos, N. M. R. Peres, and A. H. Castro Neto, Phys. Rev. Lett. **99**, 256802 (2007).

[4] P. San-Jose, J. González, and F. Guinea, Phys. Rev. Lett. **108**, 216802 (2012).

[5] A. Kerelsky, L. J. McGilly, D. M. Kennes, L. Xian, M. Yankowitz, S. Chen, K. Watanabe, T. Taniguchi, J. Hone, C. Dean, A. Rubio, and A. N. Pasupathy, Nature (London) **572**, 95 (2019).

[6] C. Lewandowski, D. Chowdhury, and J. Ruhman, Phys. Rev. B **103**, 235401 (2021).

[7] X. Kuang, Z. Zhan, and S. Yuan, Phys. Rev. B **103**, 115431 (2021).

[8] P. Novelli, I. Torre, F. H. L. Koppens, F. Taddei, and M. Polini, Phys. Rev. B **102**, 125403 (2020).

[9] V. H. Nguyen, D. Paszko, M. Lamparski, B. Van Troeye, V. Meunier, and J. C. Charlier, 2D Mater. **8**, 035046 (2021).

[10] L. A. Gonzalez-Arraga, J. L. Lado, F. Guinea, and P. San-Jose, Phys. Rev. Lett. **119**, 107201 (2017).

[11] P. J. Ledwith, E. Khalaf, and A. Vishwanath, Ann. Phys. **435**, 168646 (2021).

[12] A. Uri, S. Grover, Y. Cao, J. Â. A. Crosse, K. Bagani, D. Rodan-Legrain, Y. Myasoedov, K. Watanabe, T. Taniguchi, P. Moon, M. Koshino, P. Jarillo-Herrero, and E. Zeldov, Nature (London) **581**, 47 (2020).

[13] K. Hejazi, C. Liu, and L. Balents, Phys. Rev. B **100**, 035115 (2019).

[14] F. K. Popov and A. Milekhin, Phys. Rev. B **103**, 155150 (2021).

[15] Y. Sheffer and A. Stern, Phys. Rev. B **104**, L121405 (2021).

[16] J. A. Crosse, N. Nakatsuji, M. Koshino, and P. Moon, Phys. Rev. B **102**, 035421 (2020).

[17] P. Moon and M. Koshino, Phys. Rev. B **88**, 241412(R) (2013).

[18] H. Oka and M. Koshino, Phys. Rev. B **104**, 035306 (2021).

[19] N. Benlakhouy, A. Jellal, H. Bahlouli, and M. Vogl, arXiv:2112.13614 (2021).

[20] C. R. Dean, L. Wang, P. Maher, C. Forsythe, F. Ghahari, Y. Gao, J. Katoch, M. Ishigami, P. Moon, M. Koshino, T. Taniguchi, K. Watanabe, K. L. Shepard, J. Hone, and P. Kim, Nature (London) **497**, 598 (2013).

[21] B. Tsim, N. N. T. Nam, and M. Koshino, Phys. Rev. B **101**, 125409 (2020).

[22] M. Fujimoto and M. Koshino, Phys. Rev. B **103**, 155410 (2021).

[23] P. A. Pantaleón, T. Low, and F. Guinea, Phys. Rev. B **103**, 205403 (2021).

[24] X. Lin, B. Chen, W. Li, Z. Y. Meng, and T. Shi, arXiv:2110.00200 (2021).

[25] F. Wu, R. X. Zhang, and S. Das Sarma, Phys. Rev. Research **2**, 022010(R) (2020).

[26] Y. Fu, E. J. König, J. H. Wilson, Y. Chou, and J. H. Pixley, npj Quantum Mater. **5**, 71 (2020).

[27] M. Mirzakhani, F. M. Peeters, and M. Zarenia, Phys. Rev. B **101**, 075413 (2020).

[28] Y. Wang, G. Yu, M. Rösner, M. I. Katsnelson, H.-Q. Lin, and S. Yuan, arXiv:2110.01323 (2021).

[29] M. Fidrysiak, M. Zegrodnik, and J. Spałek, Phys. Rev. B **98**, 085436 (2018).

[30] J. Kang and O. Vafek, Phys. Rev. B **102**, 035161 (2020).

[31] K. Seo, V. N. Kotov, and B. Uchoa, Phys. Rev. Lett. **122**, 246402 (2019).

[32] M. Rodriguez-Vega, M. Vogl, and G. A. Fiete, Phys. Rev. Research **2**, 033494 (2020).

[33] M. Yankowitz, S. Chen, H. Polshyn, Y. Zhang, K. Watanabe, T. Taniguchi, D. Graf, A. F. Young, and C. R. Dean, Science **363**, 1059 (2019).

[34] C. De Beule, P. G. Silvestrov, M. Liu, and P. Recher, Phys. Rev. Research **2**, 043151 (2020).

[35] C. Xu and L. Balents, Phys. Rev. Lett. **121**, 087001 (2018).

[36] M. Rosendo López, F. Peñaranda, J. Christensen, and P. San-Jose, Phys. Rev. Lett. **125**, 214301 (2020).

[37] A. Singh and C. Benjamin, Phys. Rev. B **104**, 125445 (2021).

[38] S. A. Herrera and G. G. Naumis, Phys. Rev. B **104**, 115424 (2021).

[39] V. T. Phong, Z. Addison, S. Ahn, H. Min, R. Agarwal, and E. J. Mele, Phys. Rev. Lett. **123**, 236403 (2019).

[40] M. Koshino, N. F. Q. Yuan, T. Koretsune, M. Ochi, K. Kuroki, and L. Fu, Phys. Rev. X **8**, 031087 (2018).

[41] H. Guo, X. Zhu, S. Feng, and R. T. Scalettar, Phys. Rev. B **97**, 235453 (2018).

[42] S. Bagchi, H. T. Johnson, and H. B. Chew, Phys. Rev. B **101**, 054109 (2020).

[43] M. J. Park, H. S. Kim, and S. B. Lee, Phys. Rev. B **99**, 245401 (2019).

[44] Y. Cao, D. Rodan-Legrain, J. M. Park, N. F. Q. Yuan, K. Watanabe, T. Taniguchi, R. M. Fernandes, L. Fu, and P. Jarillo-Herrero, Sci. Adv. **372**, 264 (2021).

[45] S. Liu, E. Khalaf, J. Y. Lee, and A. Vishwanath, Phys. Rev. Research **3**, 013033 (2021).

[46] K. Kimura, M. Sigrist, and N. Kawakami, Phys. Rev. B **105**, 035130 (2022).

[47] M. Koshino and Y.-W. Son, Phys. Rev. B **100**, 075416 (2019).

[48] H. Sainz-Cruz, T. Cea, P. A. Pantaleón, and F. Guinea, Phys. Rev. B **104**, 075144 (2021).

[49] H. Ochoa and R. M. Fernandes, Degradation of phonons in disordered moiré superlattices, Phys. Rev. Lett. **128**, 065901 (2022).

[50] J. H. Wilson, Y. Fu, S. Das Sarma, and J. H. Pixley, Phys. Rev. Research **2**, 023325 (2020).

[51] Z. A. H. Goodwin, F. Corsetti, A. A. Mostofi, and J. Lischner, Phys. Rev. B **100**, 121106(R) (2019).

[52] T. Cea, P. A. Pantaleón, and F. Guinea, Phys. Rev. B **102**, 155136 (2020).

[53] P. Solís-Fernández and A. Hiroki, ACS Appl. Nano Mater. **5**, 1356 (2022).

[54] T. Vincent, K. Kawahara, V. Antonov, H. Ago, and O. Kazakova, arXiv:2107.08919 (2021).

[55] V. T. Phong, P. A. Pantaleón, T. Cea, and F. Guinea, Phys. Rev. B **104**, L121116 (2021).

[56] Y. Li, A. Eaton, H. A. Fertig, and B. Seradjeh, Phys. Rev. Lett. **128**, 026404 (2022).

[57] F. Sánchez-Ochoa, A. R. Botello-Méndez, and C. Noguez, Phys. Rev. B **104**, 075430 (2021).

[58] J. S. Hofmann, E. Khalaf, A. Vishwanath, E. Berg, and J. Y. Lee, arXiv:2105.12112 (2021).

[59] O. Vafek and J. Kang, Phys. Rev. B **104**, 075143 (2021).

[60] J. Vahedi, R. Peters, A. Missaoui, A. Honecker, and G. Trambly de Laissardière, SciPost Phys. **11**, 083 (2021).

[61] A. O. Sboychakov, A. V. Rozhkov, A. L. Rakhmanov, and F. Nori, Phys. Rev. B **100**, 045111 (2019).

[62] M. Koshino and N. N. T. Nam, Phys. Rev. B **101**, 195425 (2020).

[63] S. Carr, S. Fang, Z. Zhu, and E. Kaxiras, Phys. Rev. Research **1**, 013001 (2019).

[64] M. Angeli, D. Mandelli, A. Valli, A. Amaricci, M. Capone, E. Tosatti, and M. Fabrizio, Phys. Rev. B **98**, 235137 (2018).

[65] G. Tarnopolsky, A. J. Kruchkov, and A. Vishwanath, Phys. Rev. Lett. **122**, 106405 (2019).

[66] L. Zou, H. C. Po, A. Vishwanath, and T. Senthil, Phys. Rev. B **98**, 085435 (2018).

[67] Y. Ren, Q. Gao, A. H. MacDonald, and Q. Niu, Phys. Rev. Lett. **126**, 016404 (2021).

[68] P. J. Ledwith, A. Vishwanath, and E. Khalaf, arXiv:2109.11514 (2021).

[69] D. V. Chichinadze, L. Classen, Y. Wang, and A. V. Chubukov, arXiv:2108.05334 (2021).

[70] E. Khalaf, S. Chatterjee, N. Bultinck, M. P. Zaletel, and A. Vishwanath, Sci. Adv. **7**, eabf5299 (2020).

[71] A. O. Sboychakov, A. V. Rozhkov, A. L. Rakhmanov, and F. Nori, Phys. Rev. B **102**, 155142 (2020).

[72] Z. A. H. Goodwin, F. Corsetti, A. A. Mostofi, and J. Lischner, Phys. Rev. B **100**, 235424 (2019).

[73] G. G. Naumis, L. A. Navarro-Labastida, E. Aguilar-Méndez, and A. Espinosa-Champo, Phys. Rev. B **103**, 245418 (2021).

[74] T. Mizoguchi, Y. Kuno, and Y. Hatsugai, Phys. Rev. A **102**, 033527 (2020).

[75] T. Mizoguchi, T. Yoshida, and Y. Hatsugai, Phys. Rev. B **103**, 045136 (2021).

[76] Q.-R. Xu, V. P. Flynn, A. Alase, E. Cobanera, L. Viola, and G. Ortiz, Phys. Rev. B **102**, 125127 (2020).

[77] T. Yoshida, T. Mizoguchi, Y. Kuno, and Y. Hatsugai, Phys. Rev. B **103**, 235130 (2021).

[78] M. Ezawa, Phys. Rev. Research **2**, 033397 (2020).

[79] J. Arkinstall, M. H. Teimourpour, L. Feng, R. El-Ganainy, and H. Schomerus, Phys. Rev. B **95**, 165109 (2017).

[80] M. Yan, X. Huang, L. Luo, J. Lu, W. Deng, and Z. Liu, Phys. Rev. B **102**, 180102(R) (2020).

[81] M. Kremer, I. Petrides, E. Meyer, M. Heinrich, O. Zilberberg, and A. Szameit, Nat. Commun. **11**, 907 (2020).

[82] W. Yan, D. Song, S. Xia, J. Xie, L. Tang, J. Xu, and Z. Chen, arXiv:2110.05091 (2021).

[83] J. Kang, T. Liu, M. Yan, D. Yang, X. Huang, R. Wei, J. Qiu, G. Dong, Z. Yang, and F. Nori, arXiv:2109.00879 (2021).

[84] G. G. Naumis, Phys. Rev. B **76**, 153403 (2007).

[85] J. E. Barrios-Vargas and G. G. Naumis, J. Phys.: Condens. Matter **23**, 375501 (2011).

[86] J. Barrios-Vargas and G. G. Naumis, Solid State Commun. **162**, 23 (2013).

[87] G. G. Naumis, R. A. Barrio, and C. Wang, Phys. Rev. B **50**, 9834 (1994).

[88] G. G. Naumis, C. Wang, and R. A. Barrio, Phys. Rev. B **65**, 134203 (2002).

[89] H. K. Pal, S. Spitz, and M. Kindermann, Phys. Rev. Lett. **123**, 186402 (2019).

[90] T. M. R. Wolf, J. L. Lado, G. Blatter, and O. Zilberberg, Phys. Rev. Lett. **123**, 096802 (2019).

[91] J. Wang, Y. Zheng, A. J. Millis, and J. Cano, Phys. Rev. Research **3**, 023155 (2021).

[92] E. Khalaf, A. J. Kruchkov, G. Tarnopolsky, and A. Vishwanath, Phys. Rev. B **100**, 085109 (2019).

[93] P. J. Ledwith, G. Tarnopolsky, E. Khalaf, and A. Vishwanath, Phys. Rev. Research **2**, 023237 (2020).

[94] Y. You and A. Vishwanath, npj Quantum Mater. **4**, 16 (2019).

[95] D. Thouless, Phys. Rep. **13**, 93 (1974).

[96] F. J. Wegner, Z. Phys. B **36**, 209 (1980).

[97] R. J. Bell and P. Dean, Discuss. Faraday Soc. **50**, 55 (1970).

[98] J. Wang, J. Cano, A. J. Millis, Z. Liu, and B. Yang, Phys. Rev. Lett. **127**, 246403 (2021).

[99] J. Wang and Z. Liu, arXiv:2109.10325 (2021).

[100] S. Becker, M. Embree, J. Wittsten, and M. Zworski, Phys. Rev. B **103**, 165113 (2021).

[101] S. Becker, J. Kim, and X. Zhu, arXiv:2201.02170 (2022).